Numerical analysis of transient processes in molten carbonate fuel cells via impedance perturbations

M.Y. Ramandi [a,*], P. Berg [b], I. Dincer [a]

[a] Faculty of Engineering and Applied Science, University of Ontario Institute of Technology (UOIT), 2000 Simcoe Street North, Oshawa, Canada L1H 7K4
[b] Department of Physics, Norwegian University of Science and Technology, Trondheim 7491, Norway

HIGHLIGHTS

► A rigorous three-dimensional, transient and non-isothermal model is developed.
► A sinusoidal impedance approach is used to examine the dynamic response of the cell.
► The phase shifts and time scales of the major dynamic processes are determined.

ARTICLE INFO

ABSTRACT

In this paper, the dynamic response of a molten carbonate fuel cell is studied by means of computational fluid dynamics. First, a rigorous three-dimensional, transient and non-isothermal model is developed through a comprehensive inclusion of various transport phenomena. Next, a sinusoidal impedance approach is used to examine the dynamic response of the unit cell to inlet perturbations at impedance frequencies of 1, 0.1, 0.01 and 0.001 Hz. This analysis is further used to determine the phase shifts and time scales of the major dynamic processes within the fuel cell. The load-following capability of the unit cell is studied by examining the dynamic responses of the average current density, electrochemical reactions rates, heat and mass transfer, mass fractions and temperature. The results show that the electrochemical reactions and the charge transport process adjust within a millisecond. The mass transport process shows a comparatively larger time scale that is about 1 s. The heat transport process is the slowest process in the cell and takes about an hour to reach its steady-state. The developed model along with the dynamic analysis results can be used to design process control strategies.

1. Introduction

Molten carbonate fuel cells have been intensively studied over the past few decades, and many technical barriers have been overcome. However, cell corrosion and lifetime are still considered the greatest obstacles towards commercialization.

From an application perspective, dynamic operation has a significant effect on the cell life cycle, and hence economic matters. The MCFC behaviour in dynamic situations is still not fully understood. Specifically, when the cell undergoes voltage/load variation or fluctuation, predicting the fuel cell's dynamic performance becomes crucial. The transient situation at MCFC start-up is another example for varying conditions. Having an improved understanding of the system behaviour at dynamic phase helps to design a more robust control system in order to minimize fuel consumption and maximize operating lifetime. In fact, in order to choose an optimal control system and operation parameters, an appropriate dynamic model of MCFC consistent with other components of the hybrid system is ideal. This can be achieved by determination of time scales of the major dynamic processes in the MCFC, and their analysis and comparison with time scales of other devices in the hybrid system. The developed dynamic model can be further employed to examine quantitative responses of the system to different inlet perturbations. In addition, phase shifts between the dynamic responses of various system characteristics and the voltage perturbation will be identified.

Over the past three decades, several studies have been performed in order to develop comprehensive mathematical models representing the various processes which occur in molten carbonate fuel cell operation [1–13]. Some authors have implemented these models to investigate steady-state performance characteristics of MCFCs at cell and stack levels [14–20]. Having said that, implementation of these models in transient simulations is often subject

* Corresponding author. Tel.: +1 647 969 5880; fax: +1 905 721 3370.
E-mail addresses: Masoud.Youseframandi@uoit.ca (M.Y. Ramandi), Peter.Berg@ntnu.no (P. Berg), Ibrahim.Dincer@uoit.ca (I. Dincer).

Nomenclature

A_v	electrode active surface area ($m^2\ m^{-3}$)
c_p	specific heat ($J\ kg^{-1}\ K^{-1}$)
D	mass diffusivity ($m^2\ s^{-1}$)
E_{eq}	equilibrium electric potential (V)
F	Faraday's constant, 96,485 ($C\ mol^{-1}$)
f	frequency (Hz)
i_0	exchange current density ($A\ m^{-2}$)
i_0^0	reference exchange current density ($A\ m^{-2}$)
J	local current density ($A\ m^{-2}$)
R	volumetric current density ($A\ m^{-3}$)
k	thermal conductivity ($W\ m^{-1}\ K^{-1}$)
K	permeability (m^2)
M	molecular weight ($g\ mol^{-1}$)
n	number of electrons
P	static pressure (Pa)
R	universal gas constant ($8.314\ J\ mol^{-1}\ K^{-1}$)
S	molar entropy ($J\ mol^{-1}\ K^{-1}$)
S	source terms
t	time (s)
T	temperature (K)
$\vec{v}$	gas velocity ($m\ s^{-1}$)
X	molar fraction
Y	mass fraction

Greek letters

α	transfer coefficient
τ	tortuosity
ε	porosity
θ	electrolyte filling degree
η	overpotential (V)
μ	dynamic viscosity ($kg\ m^{-1}\ s^{-1}$)
ν	species stoichiometric coefficient of the reaction
ρ	density ($kg\ m^{-3}$)
φ	electric potential (V)
σ	electric conductivity of the solid phase ($S\ m^{-1}$)
κ	electric conductivity of the electrolyte phase ($S\ m^{-1}$)

Subscripts and superscripts

a	anode
agc	anode gas channel
c	cathode
cgc	cathode gas channel
e	electrolyte phase
g	gas phase
in	inlet
i	ith component
j	jth species
m	mass equation
out	outlet
s	solid phase
T	energy equation
u	momentum equation
ϕ_e	electronic charge equation
ϕ_c	carbonate ion charge equation
eff	effective
ref	reference state

to several simplifications. In other words, model reduction methods are widely used to establish a simple simulation model according to various operating conditions. For instance, Hao et al. [21] developed a simplified dynamic model for a cross-flow molten carbonate fuel cell and solved the model using VC++. The model was two-dimensional with uniform voltage distribution. This model was developed based on identical heat characteristics for anode, cathode and electrolyte although they typically differ by an order of magnitude. Another two-dimensional model was presented by Fermegila et al. [22] to study the effects of step change and linear ramp for various inlet conditions. The authors neglected the enthalpy transport between the electrode pores and gas phase, and also assumed an equally distributed current pattern in both electrodes (which is not always appropriate). Likewise, there exist few studies at the stack level. For instance, Lukas et al. [23] employed a lumped-parameter formulation of the first principle equations for a fuel cell stack with a simplifying assumption indicating that the solid mass temperature is equal to the exit stream temperature. In fact, this model does not provide sufficient information about the temperature profile in the electrodes and the electrolyte which is critical for MCFC lifetime and components degradation.

It was found that a three-dimensional dynamic analysis is unavailable in the literature. He and Chen [24] developed a three-dimensional transient stack model using a commercial package to demonstrate the heat transport at the stack level. However, the processes of gas transport and chemical reactions were incorporated only at the cell level.

The dynamic performance of fuel cell hybrid systems has also been investigated by some researchers. As an example, an investigation of the control performance of an internal reforming MCFC system was performed by Lukas et al. [23,25,26]. The authors used the actual data from a 2-MW demonstration project. However, the focus of this study was primarily on the molten carbonate fuel cell and the

hybrid system was not considered. Zhang et al. [27] presented a dynamic model for a hybrid fuel cell-gas turbine system with some control loops applied to the system. A distributed power generation system was studied by Grillo et al. [28]. This hybrid system is based on pressurization and heat recovering of a 100 kW molten carbonate fuel cell. Au et al. [29] investigated the optimization of MCFC operating temperatures by presenting a case study in which the efficiency of a CHP plant was analyzed. Some authors [e.g., Ref. [30]] have also used energy and exergy analyses to evaluate various system efficiencies for the integrated power generation systems.

A neural network structure approach to the dynamic performance modelling was implemented by Shen et al. [31] to model transient cell behaviour of a fuel cell. However, this model is not appropriate for other high-temperature fuel cell systems.

Recently, a transient mathematical model for a single counter-flow MCFC with an internal reformer was developed by Heidebrecht and Sundmacher [32]. Simplifications like plug flow and constant pressure in the gas phase along with a lumped solid phase for energy balance were used. Later on, this group [33] presented a more detailed study based on a dimensionless mathematical model of a single cross-flow MCFC with spatially distributed simulation results for steady-state and dynamic scenarios. This model can be applied to any other high-temperature fuel cell such as SOFC but only in two-dimensional simulation mode.

In brief, a considerable number of present studies have been carried out by either performing the simulation for individual MCFC components or by reducing the dimension to 0D (i.e. black box), 1D or 2D. In addition, many approaches have employed a uniform distribution of field variables, which significantly influences the accuracy of the dynamic results. Recently, a comprehensive three-dimensional model was developed in Ref. [34] without these simplifying assumptions. However, the focus was mainly on MCFC performance analysis.

Table 1
The geometric parameters of the simulated MCFC.

Parameter	Value
Cell length, (mm)	100
Cell width, (mm)	100
Anode gas channel height, (mm)	2.0
Anode gas channel width, (mm)	2.0
Cathode gas channel height, (mm)	2.0
Cathode gas channel width, (mm)	2.0
Anode thickness, (mm)	0.7
Anode width, (mm)	4.0
Cathode thickness, (mm)	0.6
Cathode width, (mm)	4.0
Electrolyte thickness, (mm)	1.0
Porosity of anode, ε_a [19]	0.52
Porosity of cathode, ε_c [19]	0.62

In this paper, we extend our previous work [35] to introduce a rigorous three-dimensional transient model considering a broad incorporation of various transport phenomena. The main objective of this research is to assess the non-linear dynamic response of the unit cell. In contrast to the former studies that have used 'step change' perturbation, in this study, a sinusoidal impedance approach for a variety of frequencies is integrated. In fact, there is no study on MCFC dynamic analysis based on a sinusoidal impedance approach in the open literature. Based on this analysis, the dynamic responses of various field variables and quantities are measured. Furthermore, the time scales of various transport phenomena, including mass, heat and electric charge transport processes, are determined. In addition, the phase shifts for the non-linear dynamic response of field variables and quantities such as temperature, mass fraction, current density, etc. are identified.

2. Modelling

A planar MCFC is a rectangular assembly of an electrolyte sandwiched between an anode and a cathode. The fuel gas and oxidant gas are introduced through anode gas channel (AGC) and cathode gas channel (CGC), respectively. In this arrangement, the fuel gas and oxidant flow into the porous anode and cathode where the hydrogen oxidation reaction (Equation (1)) and oxygen reduction reaction (Equation (2)) occur, respectively:

$$H_2 + CO_3^= \leftrightarrow H_2O + CO_2 + 2e^- \tag{1}$$

$$\frac{1}{2}O_2 + CO_2 + 2e^- \leftrightarrow CO_3^= \tag{2}$$

The geometric parameters of the simulated MCFC are summarized in Table 1.

2.1. Governing equations

A comprehensive MCFC model needs to consider the transport of multi-component gas species in gaseous and liquid phases, electrochemical and chemical reaction kinetics, heat generation, heat transfer, transport of electrons and carbonate ions, and porous electrode effects. These processes occur in void volumes, liquid phase, solid phase and at triple-phase boundaries (TPB). The next section provides a brief explanation of the governing equations. The reader is referred to Ramandi et al. [34] for more details.

■ Transport of gas species

In the gas phase, the governing equations include mass, momentum and species conservation:

$$\frac{\partial}{\partial t}\left(\varepsilon^{\text{eff}}\rho_g\right) + \nabla\cdot\left(\rho_g\overrightarrow{u}_g\right) = S_m \tag{3}$$

$$\frac{\partial}{\partial t}\left(\frac{1}{\varepsilon^{\text{eff}}}\rho_g\overrightarrow{u}_g\right) + \nabla\cdot\left(\frac{1}{(\varepsilon^{\text{eff}})^2}\rho_g\overrightarrow{u}_g\overrightarrow{u}_g\right) = -\nabla P_g + \nabla\cdot(\overline{\overline{\tau}}) + S_u \tag{4}$$

$$\frac{\partial}{\partial t}\left(\varepsilon^{\text{eff}}\rho_g Y_i\right) + \nabla\cdot\left(-\rho_g D_{i,m}^{\text{eff}}\nabla Y_i\right) + \nabla\cdot\left(\rho_g\overrightarrow{u}_g Y_i\right) = S_i \tag{5}$$

where ρ_g and $\overrightarrow{u}_g$ are the superficial values of the gas mixture density and velocity, respectively. The gas mixture density (kg m^{-3}) is calculated based on the ideal gas law [36]:

$$\rho_g = P_g\left(RT\sum_i\frac{Y_i}{M_i}\right)^{-1} \tag{6}$$

where P_g is the superficial value of the gas pressure (Pa), T the temperature (K), R the universal gas constant (J kmol^{-1} K^{-1}). In addition, Y_i and M_i are mass fraction and molecular weight (kg kmol^{-1}) of species i, respectively. The effective porosity (ε^{eff}) is defined using the filling degree of electrolyte and implemented in the governing equation as well as in the constitutive laws:

$$\varepsilon^{\text{eff}} = \varepsilon(1-\theta) \tag{7}$$

In addition, S_m (kg m^{-3} s^{-1}), S_u (Pa m^{-3}) and S_i (kg m^{-3} s^{-1}) are the mass, momentum and species source terms, respectively, which have different values with respect to various cell sub-domains, as given in Table 2. Also, $D_{i,m}^{\text{eff}}$ represents the effective diffusivity of species i in the gas mixture and is evaluated as

Table 2
Source terms in various conservation equations.

	S_m	S_i	S_u	S_{ϕ_s}	S_{ϕ_e}	S_T
Gas Channels	0	0	0	0	0	0
Anode	$S_{H_2} + S_{H_2O} + S_{CO_2}$	$S_{H_2} = -\frac{R_a}{nF}M_{H_2}$ $S_{H_2O} = \frac{R_a}{nF}M_{H_2O}$ $S_{CO_2} = \frac{R_a}{nF}M_{CO_2}$	$-\frac{\mu_g}{K^{\text{eff}}}\overrightarrow{u}_g$	R_a	R_a	$\frac{J_e^2}{\kappa_a} + \frac{J_s^2}{\sigma_a} + |\eta_a R_a| + |\frac{R_a}{nF}|(T\Delta S_a)$
Electrolyte	0	0	0	0	0	$\frac{J_e^2}{\kappa}$
Cathode	$S_{O_2} + S_{CO_2}$	$S_{O_2} = -\frac{R_c}{2nF}M_{O_2}$ $S_{CO_2} = -\frac{R_c}{nF}M_{CO_2}$	$-\frac{\mu_g}{K^{\text{eff}}}\overrightarrow{u}_g$	R_c	R_c	$\frac{J_e^2}{\kappa_c} + \frac{J_s^2}{\sigma_c} + |\eta_c R_c| + |\frac{R_c}{nF}|(T\Delta S_c)$

$$D_{i,m}^{\text{eff}} = \frac{1 - X_i}{\sum\limits_{i,j \neq i} \left(X_j / D_{ij}^{\text{eff}} \right)} \tag{8}$$

where D_{ij}^{eff} is the effective binary mass diffusion coefficient of species i in species j as calculated by

$$D_{ij}^{\text{eff}} = D_{ij} \frac{T}{T^{\text{ref}}} \frac{P^{\text{ref}}}{P} \frac{\varepsilon^{\text{eff}}}{\tau} \tag{9}$$

and D_{ij} is the bulk binary diffusivity at the reference temperature (T^{ref}) and reference pressure (P^{ref}). Also, τ is the tortuosity of the porous material.

■ Transport of electric charge

The governing equation for the electronic and ionic charge transport in MCFCs can be derived by means of Ohm's law as follows:

$$\nabla \cdot \left(-\sigma^{\text{eff}} \nabla \phi_s \right) = S_{\phi_s} \tag{10}$$

$$\nabla \cdot \left(\kappa^{\text{eff}} \nabla \phi_e \right) = S_{\phi_e} \tag{11}$$

where σ^{eff} and κ^{eff} are the effective electric conductivity of the solid material and liquid electrolyte, respectively. These two parameters are estimated based on the Bruggemann correlation [19] as follows:

$$\sigma^{\text{eff}} = \sigma(1 - \varepsilon) \tag{12}$$

$$\kappa^{\text{eff}} = \kappa(\varepsilon\theta)^{1.5} \tag{13}$$

The source terms on the right hand side of Equations (10) and (11) are illustrated in Table 2.

■ Transport of energy

The energy equation applying to each sub-domain of the fuel cell, can be written as [37]:

$$\frac{\partial}{\partial t} \left(\sum_{k=g,s,e} (\varepsilon\rho c_p)_k T \right) + \nabla \cdot \left(-k^{\text{eff}} \nabla T \right) + \nabla \cdot \left(\overrightarrow{u}_g \varepsilon\rho_g c_p T \right) = S_T \tag{14}$$

where k^{eff} is the effective thermal conductivity determined by

$$k^{\text{eff}} = (1 - \varepsilon)k_s + \varepsilon(1 - \theta)k_g + \varepsilon\theta k_e \tag{15}$$

Here, k_s, k_g and k_e are the thermal conductivity of the solid material, gas mixture and liquid electrolyte, respectively.

The heat generation or consumption is represented by the source term, S_T. Three kinds of heat sources are considered in the presented model, namely the reversible heat release during the electrochemical reaction, irreversible or activation heat generation and ohmic heating. Table 2 summarizes the values of energy source terms in each sub-domain.

■ Electrochemical reaction rates

All of the governing equations, described in the above sections, are strongly coupled and dependent on the electrochemical reaction rates, according to Table 2. For the anodic reaction rate, the correlation proposed by Ang and Sammels [38] is incorporated as

$$R_a = A_{v,a} \cdot i_{0,a} \left[\left(\frac{X_{H_2}}{X_{H_2,in}} \right)^{0.5} \exp\left(\frac{\alpha_{aa}F}{RT}\eta_a \right) - \left(\frac{X_{H_2}}{X_{H_2,in}} \right)^{-0.5} \left(\frac{X_{H_2O}}{X_{H_2O,in}} \right) \right.$$
$$\left. \times \left(\frac{X_{CO_2}}{X_{CO_2,in}} \right) \exp\left(-\frac{\alpha_{ca}F}{RT}\eta_a \right) \right] \tag{16}$$

Also, the superoxide mechanism [3] is employed to describe the cathodic reaction rate:

$$R_c = A_{v,c} \cdot i_{0,c} \left[\left(\frac{X_{CO_2}}{X_{CO_2,in}} \right)^{-2} \exp\left(\frac{\alpha_{ac}F}{RT}\eta_c \right) - \left(\frac{X_{CO_2}}{X_{CO_2,in}} \right)^{-0.5} \right.$$
$$\left. \times \left(\frac{X_{O_2}}{X_{O_2,in}} \right)^{0.75} \exp\left(-\frac{\alpha_{cc}F}{RT}\eta_c \right) \right] \tag{17}$$

where A_v, F and α are the electrode active surface area, Faraday constant and transfer coefficient, respectively. i_0 is the exchange current density [19] as given by

$$i_{0,a} = i_{0,a}^0 (X_{H_2,in})^{0.25} (X_{H_2O,in})^{0.25} (X_{CO_2,in})^{0.25} \tag{18}$$

$$i_{0,c} = i_{0,c}^0 (X_{O_2,in})^{0.625} (X_{CO_2,in})^{-0.75} \tag{19}$$

The overpotential, η, is defined as

$$\eta_a = \phi_s - \phi_e \tag{20}$$

$$\eta_c = \phi_s - \phi_e - E_{eq} \tag{21}$$

Moreover, E_{eq} is the potential difference between solid and electrolyte phase potentials in equilibrium, i.e. when no current is generated, and is defined using the Nernst equation [34]:

$$E_{eq} = E_0 + \left[\frac{RT}{nF} \ln\left(\frac{P_{H_2,a} P_{CO_2,c} P_{O_2,c}^{0.5}}{P_{CO_2,a} P_{H_2O,a}} \right) \right] \tag{22}$$

$$E_0 = 1.2723 - 2.7645 \times 10^{-4} T \tag{23}$$

Table 3
Physical and thermal properties of various materials.

| Parameter	Value
Thermal conductivity of anode, (W m^{-1} K^{-1}) [15,43]	78
Thermal conductivity of cathode, (W m^{-1} K^{-1}) [15,43]	0.9
Thermal conductivity of electrolyte, (W m^{-1} K^{-1}) [15]	2.0
Specific heat of anode, (J kg^{-1} K^{-1}) [44]	444
Specific heat of cathode, (J kg^{-1} K^{-1}) [44]	4435
Specific heat of electrolyte, (J kg^{-1} K^{-1}) [44]	4000
Density of anode, (kg m^{-3}) [44]	8220
Density of cathode, (kg m^{-3}) [44]	6794
Density of electrolyte, (kg m^{-3}) [44]	1914
Electric conductivity of anode, (S m^{-1}) [9,45]	1300
Electric conductivity of cathode, (S m^{-1}) [9,45]	1300
Free electrolyte conductivity: pre-exponential factor, (S m^{-1}) [2]	3637
Free electrolyte conductivity: Apparent activation energy, (K^{-1}) [2]	3016
Hydrogen diffusivity in carbon-dioxide, (m^2 s^{-1}) [44,46]	5.5E-5
Hydrogen diffusivity in water vapour, (m^2 s^{-1}) [10,44]	9.15E-5
Oxygen diffusivity in carbon-dioxide, (m^2 s^{-1}) [9,46]	1.4E-5
Oxygen diffusivity in nitrogen, (m^2 s^{-1}) [44,46]	1.8E-5
Carbon-dioxide diffusivity in water vapour, (m^2 s^{-1}) [44,46]	1.62E-5
Carbon-dioxide diffusivity in nitrogen, (m^2 s^{-1}) [44,46]	1.6E-5
Hydrogen diffusivity in liquid electrolyte, (m^2 s^{-1}) [47]	1E-7
Oxygen diffusivity in liquid electrolyte, (m^2 s^{-1}) [36,47]	3E-7
Carbon-dioxide diffusivity in liquid electrolyte, (m^2 s^{-1}) [36,47]	1E-7
Water vapour diffusivity in liquid electrolyte, (m^2 s^{-1})	1E-7
Nitrogen diffusivity in liquid electrolyte, (m^2 s^{-1})	1E-7
Standard entropy change of anode, (J mol^{-1} K^{-1}) [48]	54.56
Standard entropy change of cathode, (J mol^{-1} K^{-1}) [48]	−216.2
Standard entropy change of generation reaction, (J mol^{-1} K^{-1}) [48]	−161.64
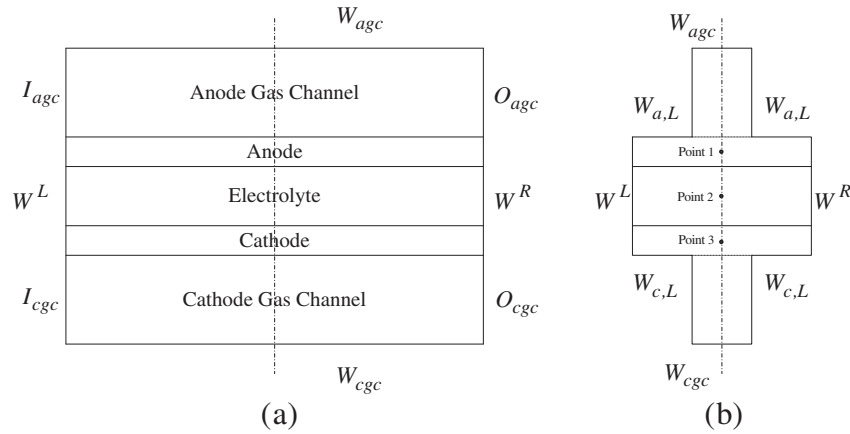
Fig. 1. Boundary conditions for the MCFC model: (a) down the channel view, (b) cross-sectional view.

The physical and thermal properties that are employed in the developed model, are listed in Table 3.

2.2. Boundary and initial conditions

(i) Boundary conditions

A complete set of boundary conditions is required for the governing equations formulated in the previous section. It should be specified involving the transport of gas species, energy, electrons and carbonate ions. A demonstration of the various internal and external boundaries is presented in Fig. 1. The boundary conditions are required only at the external surfaces of the computational domain due to the implemented single-domain formulation

■ At AGC inlet (I_{agc}) and CGC inlet (I_{cgc})

The gas species mass fraction, total mass flux and temperature of the entering gas flow are specified. Furthermore, the normal fluxes of all other variables are set to zero.

$$\left\{ \begin{array}{l} Y_i = \text{Specified} \\ \dot{m} \cdot \vec{n} = \text{Specified} \\ T = \text{Specified} \\ \dfrac{\partial \Theta}{\partial \vec{n}} = 0 \end{array} \right\} \tag{24}$$
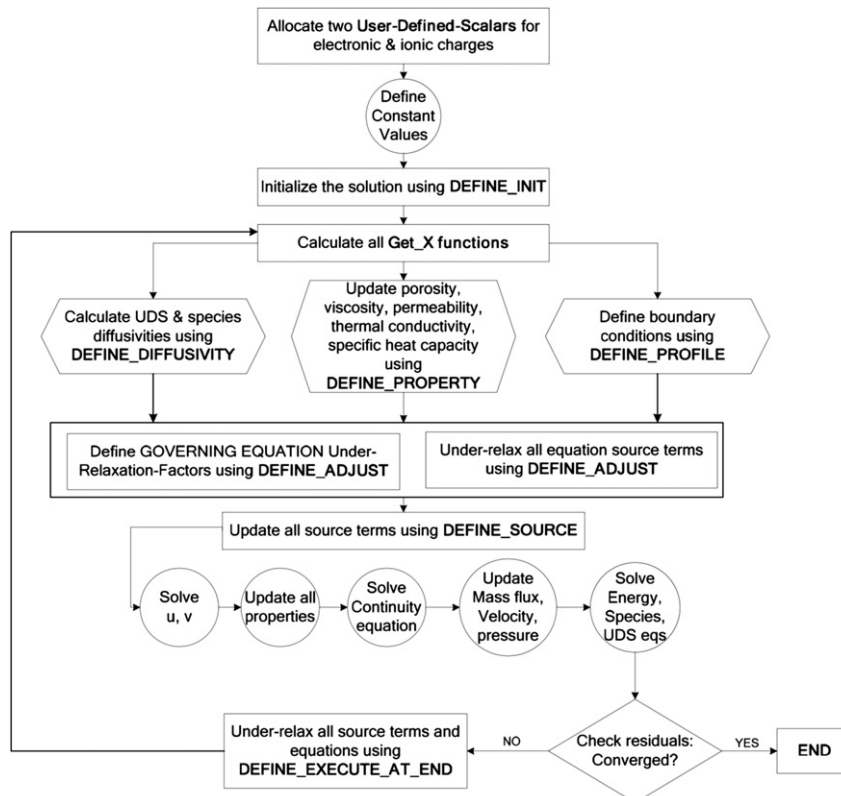
Fig. 2. Illustration of the modified solution procedure based on the developed in-house code, implemented in ANSYS FLUENT.
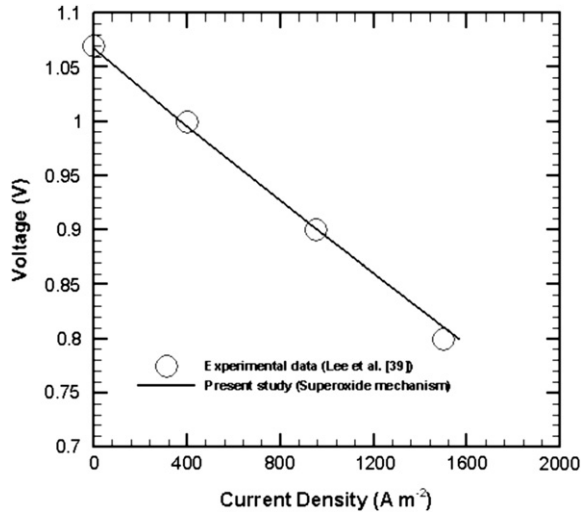
Fig. 3. Model parameter verification: using the experimental study by Lee et al. [39].

Θ represents any remaining variable which is not explicitly specified.

■ At AGC outlet (O_{agc}) and CGC outlet (O_{cgc})

Since the gas channels aspect ratio is very large, the flow is assumed to be fully developed. This means that none of the variables and respective fluxes varies in the normal direction. In addition, the gas pressure is specified.

$$\left\{ \begin{array}{l} P = \text{Specified} \\ \dfrac{\partial \Theta}{\partial \overrightarrow{n}} = 0 \end{array} \right\} \tag{25}$$

■ At AGC walls (W_{agc}) and CGC walls (W_{cgc})

A no-slip boundary condition is applied to these walls along with a zero-flux boundary condition for all other variables.
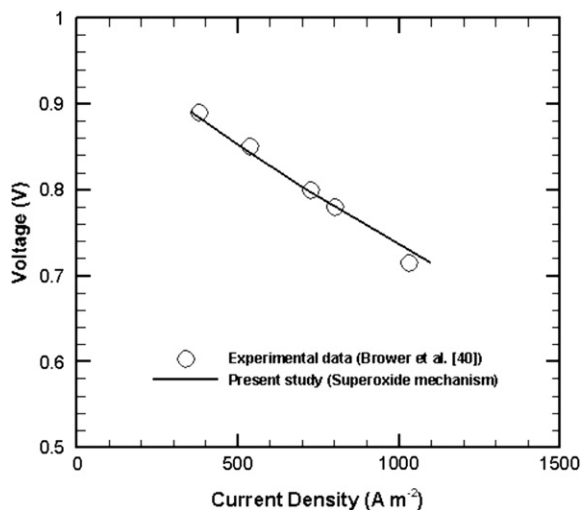
Fig. 4. Model validation: using the experimental and numerical study by Brouwer et al. [40].
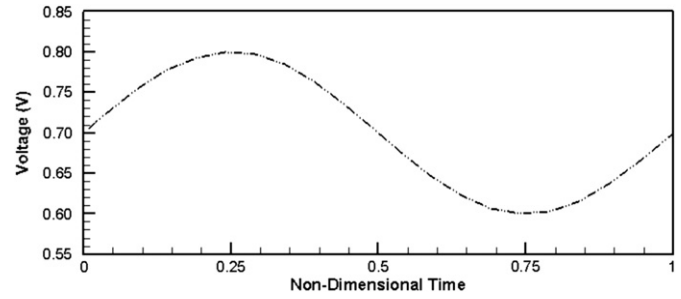
Fig. 5. The applied sinusoidal voltage perturbation with amplitude of 0.1 V under different impedance frequencies (10.0–0.001 Hz) during one sinusoidal cycle. The horizontal axis represents dimensionless time.

$$\left\{ \begin{array}{l} \overrightarrow{u}_g = 0 \\ \dfrac{\partial \Theta}{\partial \overrightarrow{n}} = 0 \end{array} \right\} \tag{26}$$

■ At anode lands ($W_{a,L}$)

The electronic potential is set to zero. The flux of ionic charge and all remaining variables are set to zero.

$$\left\{ \begin{array}{l} \phi_s = 0 \\ \dfrac{\partial \Theta}{\partial \overrightarrow{n}} = 0 \end{array} \right\} \tag{27}$$

■ At cathode lands ($W_{c,L}$)

The electronic potential is set to be the cell voltage. The flux of ionic charge and all remaining variables are set to zero.

$$\left\{ \begin{array}{l} \phi_s = V \\ \dfrac{\partial \Theta}{\partial \overrightarrow{n}} = 0 \end{array} \right\} \tag{28}$$

■ At no-flux boundaries (W^L and W^R)

The zero-flux condition is assumed for all variables.

$$\left\{ \dfrac{\partial \Theta}{\partial \overrightarrow{n}} = 0 \right\} \tag{29}$$

(ii) Initial conditions

For the case of sinusoidal voltage perturbation, the initial conditions are considered to be the steady-state simulation results with the same model input parameters.
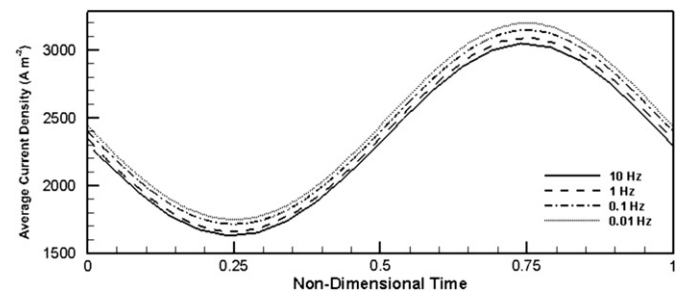

Fig. 6. The applied sinusoidal voltage perturbation with amplitude of 0.1 V under different impedance frequencies (10.0–0.01 Hz) during one sinusoidal cycle.

3. Numerical study

The computational domain is divided into a number of control volumes using ANSYS ICEM CFD 12.0.1. The Finite Volume based commercial software, ANSYS FLUENT 12.0.1, is employed to discretize and solve the set of governing equations. These equations are strongly coupled through the source terms resulting from the electrochemical reactions. A set of under-relaxation techniques is developed to handle the divergence difficulties. Furthermore, the C programming language is used to develop a supplemental code in order to include several capabilities (e.g. non-standard transport equations, source terms, temperature dependent properties, etc.) to ANSYS FLUENT 12.0.1. The SIMPLE algorithm is implemented for the coupling between the pressure and velocity field. An algebraic multi-grid (AMG) method with a Gauss–Seidel type smoother is used to accelerate the convergence. A strict convergence criterion with a residual of 10^{-10} is used for all variables. The solution procedure is illustrated in Fig. 2.

4. Results and discussion

4.1. Model validation

First of all, for a specific case, available experimental data was used to adjust model input parameters (Fig. 3). Then, the validated model was employed to check the validity of the results by conducting a comparison with an experimental study and satisfactory agreement was achieved (Fig. 4).

4.2. Non-linear impedance load change

The various transport phenomena in a molten carbonate fuel cell have a broad range of time scales. It is acknowledged that the electrochemical reactions at the three-phase boundaries in the anode and cathode, heat conduction in solid electrodes and electrolyte, convective form of heat and mass transfer in gas channels, and charge transport processes at the electrodes and inside the electrolyte are the dominant processes which take place inside an MCFC. To be able to elucidate the phase shifts and time scales for different processes occurring in the MCFCs, a transient technique is incorporated into the mathematical model.

In this approach, a sinusoidal (i.e. non-linear) voltage perturbation is applied to assess the resulting harmonic response of current density, outlet mass flow rates, heat transfer rates, mass fractions and temperatures. The general form of the applied voltage is

$$V(t) = V_b + A\sin(2\pi ft) \tag{30}$$

This sinusoidal functional serves as the boundary condition for the solid phase potential at the cathode land boundaries (in Equation (28)):
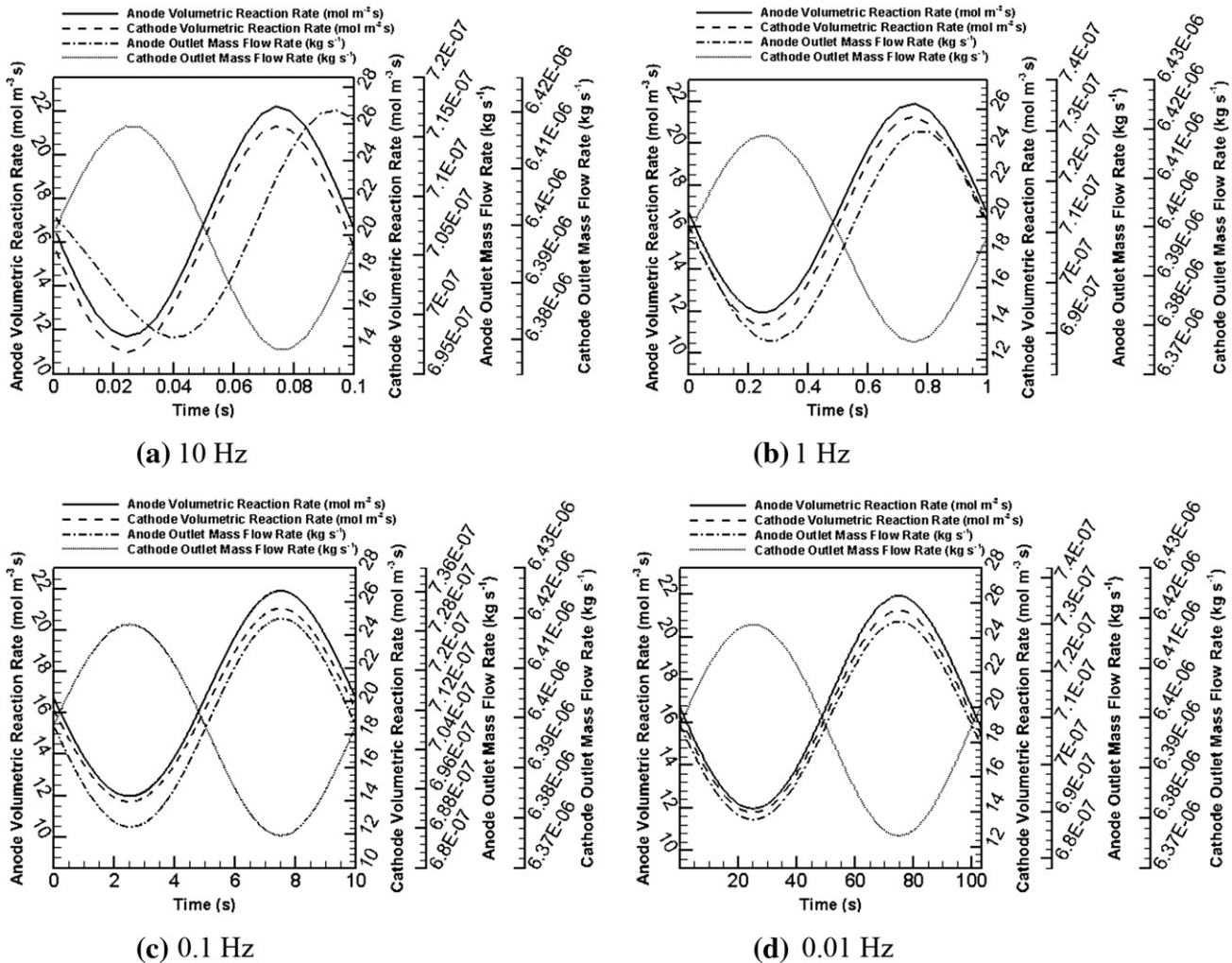

Fig. 7. Dynamic response of the electrodes volumetric reaction rates and gas flow rates at gas channel outlets corresponding to sinusoidal voltage perturbation during one sinusoidal cycle and over a wide range of impedance frequencies (10.0–0.01 Hz).

$$\phi_s = V(t) \tag{31}$$

In this equation, V_b is the base voltage, A is the amplitude of the voltage perturbation, f is the frequency of the sine wave and t is the operating time.

Using the boundary condition described in Equations (30) and (31) and keeping all other input quantities constant, several simulations were carried out in transient mode. The results demonstrate the non-linear dynamic responses of the unit cell variables.

Generally, if the amplitude of the applied perturbation is small enough, the dynamic responses are also sinusoidal (although this may not be applicable for the energy (heat) transport process in MCFCs). Accordingly, the dynamic response of an affected field variable, Θ, is

$$\Theta = \Theta_b + A_\Theta \sin(2\pi f t + \theta(f)) \tag{32}$$

where $\theta(f)$ is the phase difference between the voltage and the response function. Obviously, for a purely resistive behaviour θ is zero.

In this study, the following parameters are utilized to analyze the non-linear dynamic responses:

$$V_b = 0.7 \text{ V}$$

$$A = 0.1 \text{ V}$$

$$f = 0.001, \ 0.01, \ 0.1, \ 1.0, \ 10.0 \text{ Hz}$$

Fig. 5 demonstrates the sinusoidal perturbation for all frequencies over one periodic cycle. In this figure, the horizontal axis is the non-dimensional time which is defined as:

$$\text{Non – dimensional time} = \frac{\text{Time(s)}}{\text{One periodic cycle(s)}} \tag{33}$$

By this definition, the applied sinusoidal voltage versus non-dimensional time follows identical shapes for all frequencies. Accordingly, 0.50 along the horizontal axis corresponds to 500 s, 50 s, 5 s, 0.5 s and 0.05 s for the impedance frequencies of 0.001 Hz, 0.01 Hz, 0.1 Hz, 1 Hz and 10 Hz, respectively.

Hereafter, Fig. 5 along with the resulting dynamic responses will be utilized to determine the phase shifts among the different variables and the applied perturbation. Nevertheless, the characteristic time scale of each process will also be assessed.

The most critical parameter in the dynamic response analysis of fuel cells is the average cell current density. The corresponding time scale characterizes the charge transport in both solid and electrolyte phase and can be evaluated by [41]:

$$\tau_{charge} = \delta^2 A_v C \left(\frac{1}{\sigma} + \frac{1}{\kappa} \right) \tag{34}$$
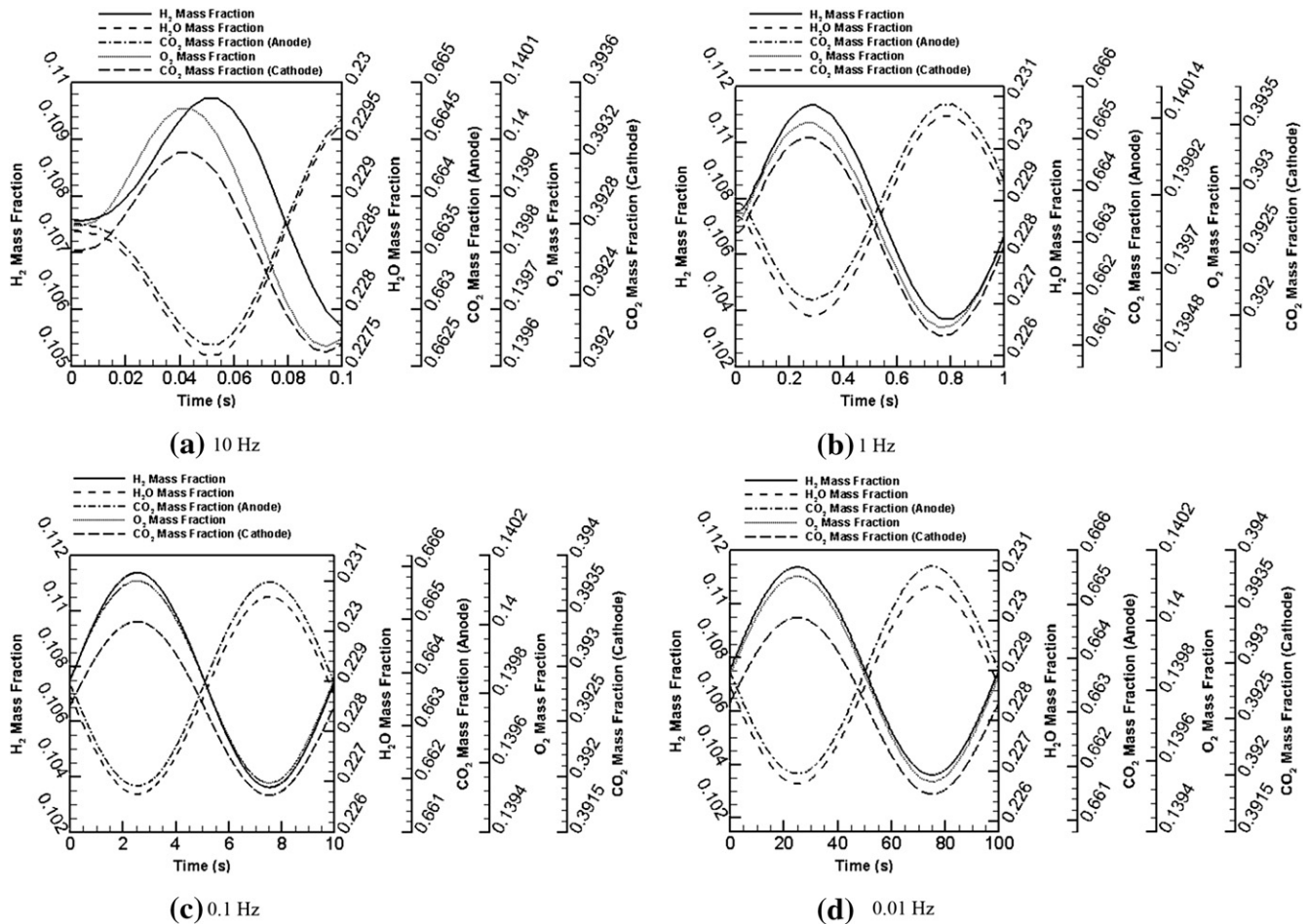

Fig. 8. Dynamic response of the gas species mass fractions corresponding to sinusoidal voltage perturbation during one sinusoidal cycle and over a wide range of impedance frequencies (10.0−0.01 Hz).

where δ is the electrode thickness and C is the capacity which ranges from 1.5 to 55 F m^{-2} [42]. Using the model input parameters, the time scale of the charge transport process is evaluated to be 3.6E-06 to 1.5E-04 s. These values imply that the charge transport in MCFCs is very fast. Using the evaluated time step size, the transient technique is employed to provide an improved understanding of the charge transport process. Fig. 6 shows the dynamic responses of the unit cell average current density during one sinusoidal cycle under four different frequencies (0.01–10 Hz). It may be observed that the

resulting dynamic responses for all impedance frequencies follow a sinusoidal trend with no noticeable phase shifts. This simply entails that the dynamic response of the cell current density is independent of the perturbation frequency. Technically, this occurs only when the associated time scale is extremely small.

The next parameters of interest are the anode and cathode volumetric reaction rates which are demonstrated in Fig. 7 for various frequencies. This figure exhibits a pattern similar to the average current density with no phase shift. It seems as if the
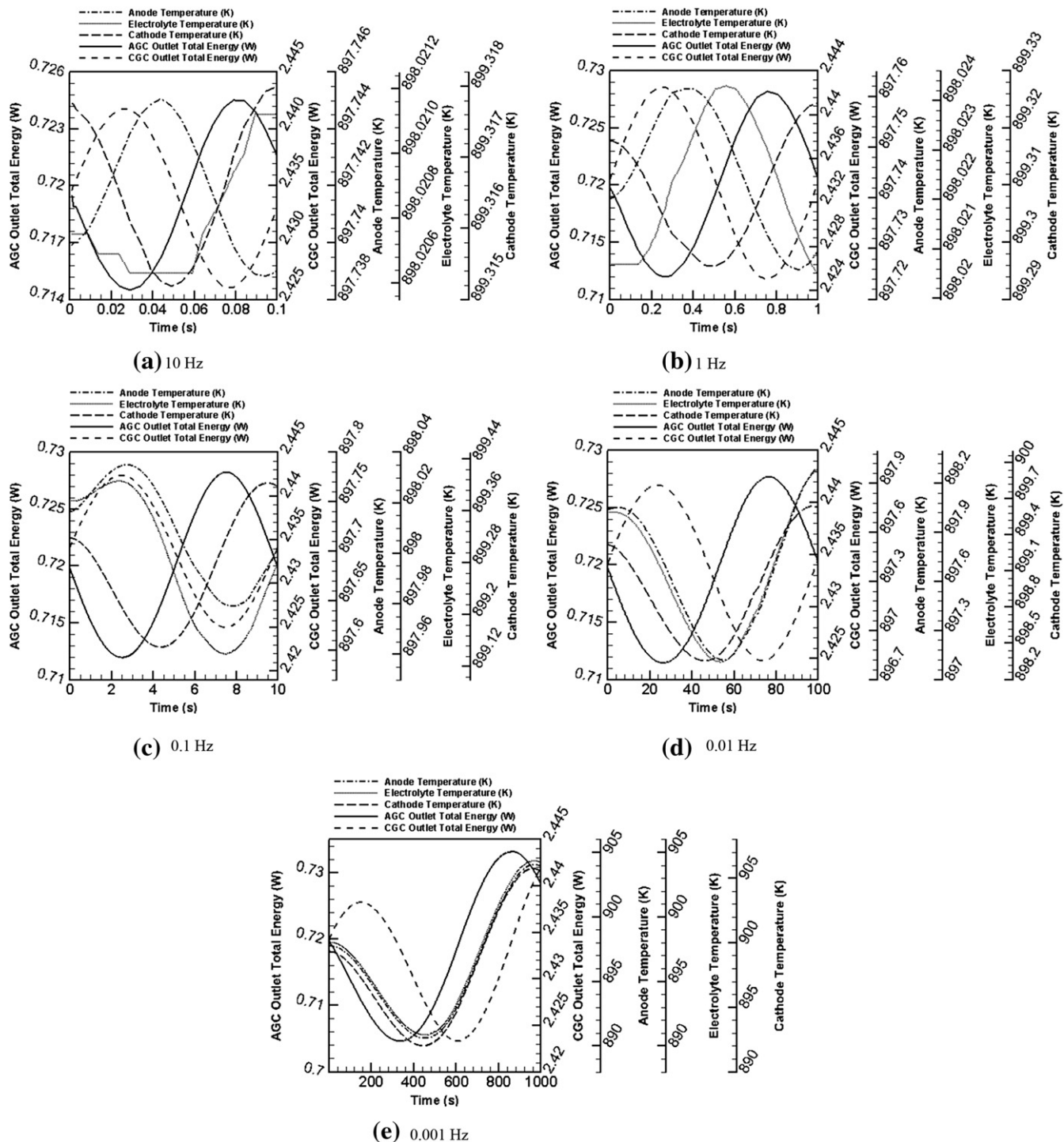

Fig. 9. Dynamic response of electrolyte and electrodes' temperature and outlet energy corresponding to sinusoidal voltage perturbation during one sinusoidal cycle and over a wide range of impedance frequencies (10.0–0.001 Hz).

electrochemical reaction rates respond to the voltage change instantaneously. This is expected because the charge transport process which exhibited an extremely small time scale is coupled with the electrochemical reactions. In other words, the ionic and electronic charges are generated and consumed on the same time scales as the charge transport process.

In order to identify the dynamic behaviour of the mass transport process, two types of parameters are considered. One is the average bulk value of mass flow rates at gas channel outlets (shown in Fig. 7), and the second (Fig. 8) is the local value of the gaseous species mass fractions in the anode and cathode (at Points 1 and 3, shown in Fig. 1). The approximate characteristic time scale is then evaluated as

$$\tau_{mass} = \frac{\delta^2}{D_g^{\text{eff}}}, \tag{35}$$

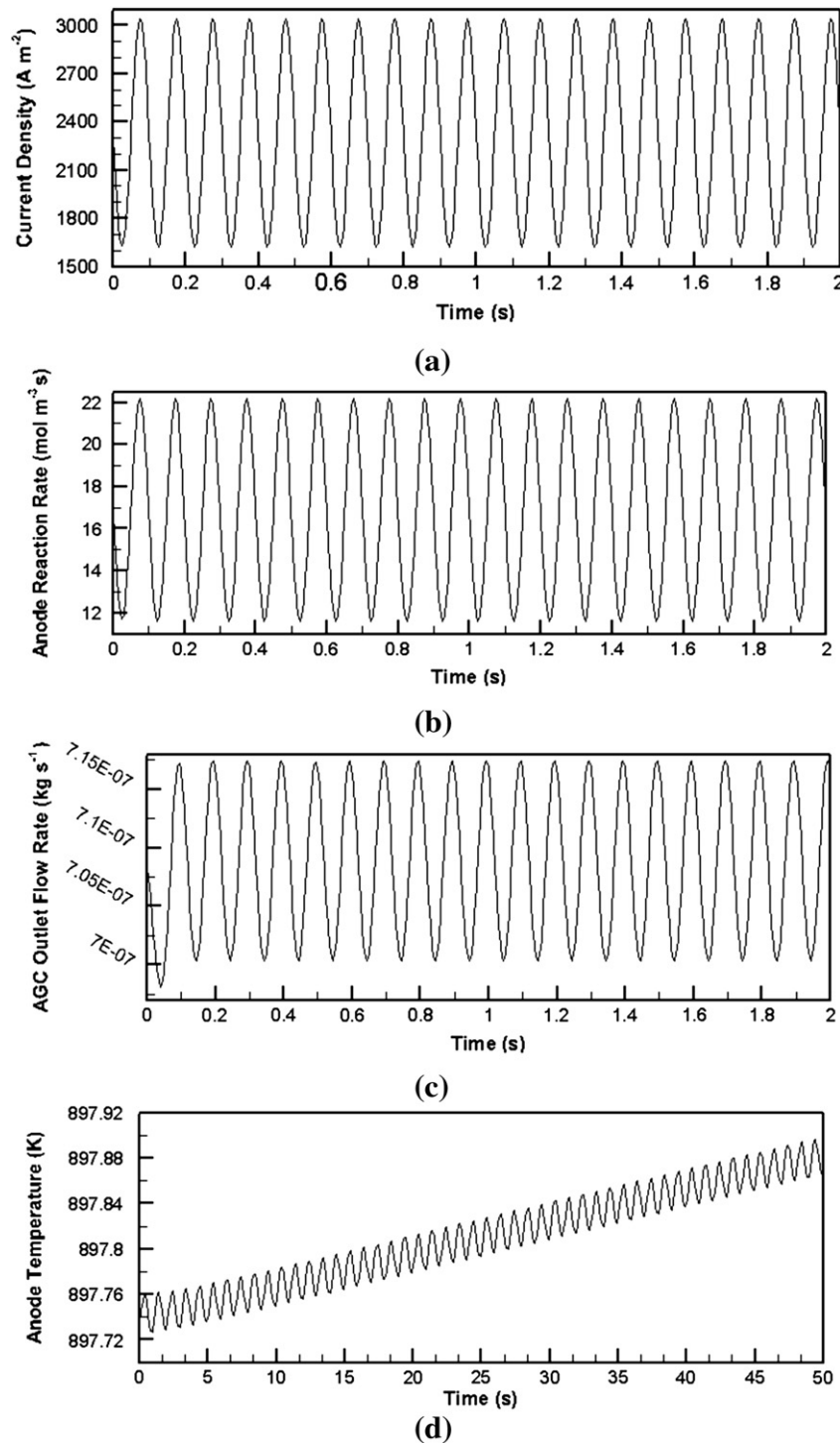assuming that diffusion within the electrode dominates the mass transport.

Fig. 10. Time-extended dynamic response of average current density, anode reaction rate, AGC outlet mass flow rate (at 10 Hz) and anode temperature (at 1 Hz).

By substituting the parameter values, the time scale of the gas transport process is evaluated to be about 0.2–1 s. This value indicates that the gas transport process is slower than the electrochemical reactions and the charge transport process. Fig. 7 confirms this conclusion by showing obvious phase shifts for both AGC and CGC outlet mass flow rates at the frequency of 10 Hz. These phase shifts then decrease and vanish at a frequency of 1 Hz. One can justify the fading of the phase shift by taking into account the sluggishness of the variation in the operating condition, when the oscillation frequency is small. In this situation, the unit cell has more time to reach its local equilibrium. Therefore, the phase shift disappears when the impedance frequency diminishes. Even though the AGC and CGC outlet mass flow rates (bulk variables) are reasonable parameters for analysis of the mass transport characteristic time scales, a number of local variables are also selected to present an enhanced understanding of mass transport process. Results are summarized in Fig. 8, confirming the same time scales as that of the bulk variables.

Finally, the characteristic time scale of the energy (heat) transport process is examined. It can be evaluated as

$$\tau_{energy} = \frac{\rho c_p \delta^2}{k} \qquad (36)$$

It is worthwhile to mention that there are two major energy transport mechanisms in an MCFC. One is the convective heat transfer in gas channels, and the other is the heat conduction in electrodes and the electrolyte. The overall energy transport process is controlled by the slowest mechanism which has the largest time scale. Since the heat capacity of the solid material is much higher than the heat capacity of the gas mixture, the parameters in Equation (36) are replaced by the solid material properties. Thus, the characteristic time scale is found to be of the order of 1000 s. This value shows that the energy transport process is three orders of magnitude slower than the mass transport process. This notable conclusion facilitates the process of choosing the appropriate time step size. Transient simulations must be started with an extremely small time step size (1.0E-6.0 s) which can be increased up to 1 s when the operating time passes the mass transport time scale. This way, solution accuracy is secured along with optimal computational expense.

Similar to the mass transport dynamic response, both local and bulk variables are chosen to analyze the phase shifts for energy transport characteristics. Fig. 9 shows the resulting dynamic response of the local temperature (at Points 1, 2 and 3 in Fig. 1) and the average bulk value of total energy at gas channel outlets. It may be observed that there is more complexity in the dynamic responses corresponding to the energy transport process. First of all, the electrolyte temperature does not exhibit a simple sinusoidal shape at high frequencies (10 Hz and 1 Hz in Fig. 9a and b). This underlines that the heat conduction process in the electrolyte has the largest time scale and hence is the slowest thermal process in the unit cell. One may associate this with the heat conductivity or the heat capacity of the electrolyte. However, the sluggishness of this process can only be justified by Equation (36) which shows the largest value for the electrolyte time scale. Nonetheless, as the impedance frequency decreases, the electrolyte temperature dynamic response recovers the sinusoidal shape. Additionally, there are obvious phase shifts for all frequencies (Fig. 9a–d) regarding the dynamic responses of the four variables. Therefore, another simulation was carried out to examine the dynamic response with a much smaller frequency (0.001 Hz). Results are shown in Fig. 9e. Even at this small frequency, the thermal characteristics of the unit cell do not show a rapid response to the voltage perturbation. Also, the local and bulk values of the investigated variables and parameters demonstrate different phase shifts indicating their different characteristic time scales. The phase shifts can be predicted to disappear at frequencies
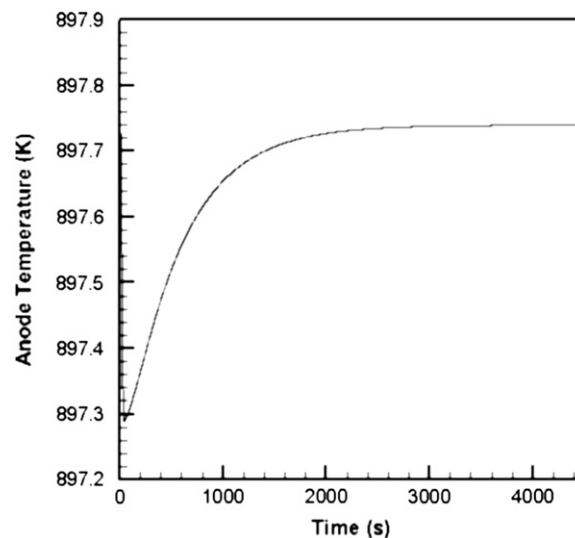

Fig. 11. Linear dynamic response of the anode temperature to a small change in the operating voltage.

under 0.0005 Hz. This conclusion reveals the large time scale of the energy transport process to be 2500 s. This great hindrance of the dynamic response, in comparison with the mass and charge transport processes, is primarily because of the high thermal capacity of the fuel cell. This feature can be beneficial for the design of control systems for MCFC-hybrid plants.

Figs. 7–9 show that the majority of the chemical and physical processes in an MCFC occur in the first second of operation. Only heat transport takes longer to reach its local equilibrium. Therefore, the same impedance simulation was extended for 20 cycles at a frequency of 10 Hz to study the dynamic responses of the fast and very fast processes. This large frequency is required to capture the transient period. However, for the sake of comparison, only a few variables are selected for the extended time study. Results are summarized in Fig. 10a–c. It may be observed that the average cell current density (Fig. 10a) and anode reaction rate (Fig. 10b) respond to the voltage fluctuation instantaneously without any obvious phase shift. On the other hand, the response of the AGC outlet mass flow rate (Fig. 10c) is relatively slower. A 0.2 s transition time is required for the outlet flow rate to reach the steady-state condition. The last part of Fig. 10 (10d) demonstrates the anode temperature response for the first 50 cycles at an impedance frequency of 1 Hz. This small frequency is necessary because the energy transport process is a much slower process. Fig. 10d shows that the oscillation amplitude of the anode temperature increases instantly, and has a continuous growing trend throughout the operation time. This simulation was further continued for the next 1000 s and the same rising trend was observed. Due to the enormous number of cycles over the extended operation time, the resulting graph is not readable and helpful. Thus, it is not included in this study.

In its place, a new simulation, with a linear voltage change during the initial phase of the operation, was carried out and the results are demonstrated in Fig. 11. This figure shows the anode temperature variation over a time period of 4500 s. It confirms the previous conclusion (from Fig. 9e) that the transition period of the energy transport process is about 2500 s.

5. Conclusions

A three-dimensional transient mathematical model for a MCFC was developed to study the dynamic response of the fuel cell.

ANSYS FLUENT 12.0.1, a finite volume based commercial software package, was utilized to solve the system of partial differential equations. A sinusoidal impedance approach was employed to identify the characteristic time scales for the major dynamic transport processes. Thus, the electrochemical reactions, charge transport, mass transport and energy transport processes were analyzed to find the cell response during a sinusoidal voltage change and over a wide range of impedance frequencies. The corresponding time scales were verified numerically with distinctive order of magnitudes, giving us confidence in our model and numerical solutions. The majority of the physical and electrochemical processes occur in the first second of the operation. The anodic and cathodic electrochemical reactions along with the charge transport process were found to be the fastest processes in the unit cell with time scales about 10^{-6}–10^{-4} s. The time scale of the gas transport process was evaluated to be in order of 1 s, while the energy transport process exhibited a time scale larger than 1000 s. This is in agreement with experimental data provided internally by Enbridge Inc. [49]. Hence, a variable step size algorithm was employed to increase the efficiency of our computations.

Having established a functional transient model and code, future work will employ the developed model along with the dynamic analysis result to design more robust process control strategies for MCFC-hybrid systems. This work will also be used as a first step to design a diagnosis tool in thermal-stress analysis to determine degradation effects, and may help to extend the life cycle of the fuel cell.

Acknowledgements

References

[1] C.Y. Yuh, J.R. Selman, Journal of Electrochemical Society 131 (1984) 2062–2069.
[2] G. Wilemski, Journal of the Electrochemical Society 130 (1983) 117–121.
[3] H.R. Kunz, L.J. Bergoli, T. Szymanski, Journal of Electrochemical Society 131 (1984) 2815–2821.
[4] J. Jewulski, L. Suski, Journal of Applied Electrochemistry 14 (1984) 135–143.
[5] J. Jewulski, Journal of Applied Electrochemistry 16 (1986) 643–653.
[6] G.L. Lee, J.R. Selman, L. Plomp, Journal of the Electrochemical Society 140 (1993) 390–396.
[7] E. Fontes, C. Lagergren, D. Simonsson, Electrochimica Acta 38 (1993) 2669–2682.
[8] J.A. Prins-Jansen, K. Hemmes, H.W. De Wit, Electrochimica Acta 42 (1997) 3585–3600.
[9] E. Fontes, M. Fontes, D. Simonsson, Electrochimica Acta 41 (1996) 1–13.
[10] E. Fontes, C. Lagergren, G. Lindbergh, D. Simonsson, Journal of Applied Electrochemistry 27 (1997) 1149–1156.
[11] J.D. Fehribach, J.A. Prins-Jansen, K. Hemmes, J.H.W. De Wit, F.W. Call, Journal of Applied Electrochemistry 30 (2000) 1015–1021.
[12] J.D. Fehribach, K. Hemmes, Journal of Electrochemical Society 148 (2001) A783–A787.
[13] J.D. Fehribach, European Journal of Applied Mathematics 12 (2001) 77–96.
[14] M.J. Yoo, D.P. Kim, G.Y. Chung, H.C. Lim, Journal of Fuel Cell Science and Technology 3 (2006) 327–332.
[15] J.H. Wee, K.Y. Lee, International Journal of Energy Research 30 (2006) 599–618.
[16] J.H. Wee, K.Y. Lee, International Journal of Energy Research 30 (2006) 619–631.
[17] Y.J. Kim, I.G. Chang, T.W. Lee, M.K. Chung, Fuel 89 (2010) 1019–1028.
[18] M. Sparr, A. Boden, G. Lindbergh, Journal of the Electrochemical Society 153 (2006) A1525–A1532.
[19] A. Boden, G. Lindbergh, Journal of the Electrochemical Society 153 (2006) A2111–A2119.
[20] F. Yoshiba, T. Abe, T. Watanabe, Journal of Power Sources 87 (2000) 21–27.
[21] H. Hao, H. Zhang, S. Weng, M. Su, Journal of Power Sources 161 (2006) 849–855.
[22] M. Fermegila, A. Cudicio, G. De Simon, G. Longo, S. Pricl, Fuel Cells 5 (2005) 66–79.
[23] M.D. Lukas, K.Y. Lee, Fuel Cells 5 (2005) 115–125.
[24] W. He, Q. Chen, Journal of Power Sources 73 (1998) 182–192.
[25] M.D. Lukas, K.Y. Lee, H. Ghezel-Ayagh, IEEE Transaction on Energy Conversion 14 (1999) 1651–1657.
[26] M.D. Lukas, K.Y. Lee, H. Ghezel-Ayagh, Control Engineering Practice 10 (2002) 197–206.
[27] H. Zhang, S. Weng, M. Su, W. Zhang, Journal of Fuel Cell Science and Technology 7 (2010) 061006-1–061006-8.
[28] O. Grillo, L. Magistri, A.,F. Massardo, Journal of Power Sources 115 (2003) 252–267.
[29] S.F. Au, S.J. McPhail, N. Woudstra, K. Hemmes, Journal of Power Sources 122 (2003) 37–46.
[30] R. Rashidi, P. Berg, I. Dincer, International Journal of Hydrogen Energy 34 (2009) 4395–4405.
[31] C. Shen, G.Y. Cao, X.J. Zhu, Simulation Modelling Practice and Theory 10 (2002) 109–119.
[32] P. Heidebrecht, K. Sundamacher, Chemical Engineering Science 58 (2003) 1029–1036.
[33] P. Heidebrecht, K. Sundamacher, Journal of the Electrochemical Society 152 (2005) A2217–A2228.
[34] M.Y. Ramandi, I. Dincer, Journal of Power Sources 196 (2011) 8509–8518.
[35] M.Y. Ramandi, P. Berg, I. Dincer, Journal of Power Sources 218 (2012) 192–203.
[36] R.B. Bird, W.E. Stewart, E.N. Lightfoot, Transport Phenomena, John Wiley & Sons, New York, 1960.
[37] C.Y. Wang, Chemical Reviews 104 (12) (2004) 4727–4766.
[38] P.G.P. Ang, A.F. Sammells, Journal of Electrochemical Society 127 (1980) 1287–1294.
[39] C. Lee, D. Kim, H. Lim, Journal of Electrochemical Society 154 (2007) B396–B404.
[40] J. Brouwer, F. Jabbari, E. Martins Leal, T. Orr, Journal of Power Sources 158 (2006) 213–224.
[41] H. Wu, X. Li, P. Berg, International Journal of Hydrogen Energy 32 (2007) 2022–2031.
[42] P. Heidebrecht, Modelling, Analysis and Optimisation of a Molten Carbonate Fuel Cell with Direct Internal Reforming (DIR-MCFC), PhD thesis, Otto-von-Guericke University Magdeburg, 2004.
[43] Z. Ma, S.M. Jeter, A.I. Abdel-Khalik, International Journal of Hydrogen Energy 28 (2003) 85–97.
[44] W.M. Haynes (Ed.), CRC Handbook of Chemistry and Physics, 91st ed., CRC Press/Taylor and Francis, 2011 (Internet Version).
[45] Y.S. Xu, Y. Liu, X.Z. Xu, G.X. Huang, Journal of the Electrochemical Society 153 (2006) A607–A613.
[46] X. Li, Principles of Fuel Cells, Taylor & Francis, New York, 2005.
[47] N. Subramanian, B.S. Haran, P. Ganesan, R.E. White, B.N. Popov, Journal of the Electrochemical Society 150 (2003) A46–A56.
[48] F. Yoshiba, International Journal of Energy Research 28 (2004) 1361–1377.
[49] Enbridge Inc., Internal Communications (2011).